ORIGINAL ARTICLE

Chengjie Wang · Jeff D. Eldredge

Low-order phenomenological modeling of leading-edge vortex formation

Abstract A low-order point vortex model for the two-dimensional unsteady aerodynamics of a flat plate wing section is developed. A vortex is released from both the trailing and leading edges of the flat plate, and the strength of each is determined by enforcing the Kutta condition at the edges. The strength of a vortex is frozen when it reaches an extremum, and a new vortex is released from the corresponding edge. The motion of variable-strength vortices is computed in one of two ways. In the first approach, the Brown–Michael equation is used in order to ensure that no spurious force is generated by the branch cut associated with each vortex. In the second approach, we propose a new evolution equation for a vortex by equating the rate of change of its impulse with that of an equivalent surrogate vortex with identical properties but constant strength. This impulse matching approach leads to a model that admits more general criteria for shedding, since the variable-strength vortex can be exchanged for its constant-strength surrogate at any instant. We show that the results of the new model, when applied to a pitching or perching plate, agree better with experiments and high-fidelity simulations than the Brown–Michael model, using fewer than ten degrees of freedom. We also assess the model performance on the impulsive start of a flat plate at various angles of attack. Current limitations of the model and extensions to more general unsteady aerodynamic problems are discussed.

1 Introduction

The leading-edge vortex (LEV), a harbinger of incipient stall in fixed-wing flight at large angle of attack, is well known to provide a short-term enhancement of the lift while it remains attached to the wing. Since the underlying wing motion in biological mechanisms of flight (e.g., flapping, pitch-up, etc.) generally occurs on a smaller time scale than the development of full stall, this enhancement provided by the LEV is often exploited by small airborne creatures. Therefore, in the general spirit of distilling these mechanisms for use in agile micro air vehicles (MAVs), it is useful to understand the characteristics of the LEV, and in particular, to develop tools to describe its dynamics.

The process of dynamic stall in which the LEV generally appears has been well studied in various aerodynamic contexts, for example, in retreating helicopter rotor blades and highly maneuverable aircraft, and there is a correspondingly rich body of literature on the subject [17,25,28,47]. In particular, in the context of MAV flight, there has been a number of recent studies of a flat plate pitching at constant rate to large angle of attack,

Communicated by T. Colonius.

C. Wang · J. D. Eldredge (✉)
Mechanical and Aerospace Engineering Department, University of California Los Angeles,
420 Westwood Plaza, Los Angeles, CA 90095-1597, USA
E-mail: eldredge@seas.ucla.edu
Tel.: +1-310-206-5094
Fax: +1-310-206-4830

carried out both experimentally and computationally [12,16,19,35]. These studies have collectively revealed many of the fundamental characteristics of the LEV in response to the pitch rate, initial acceleration, and pitch axis.

In spite of these studies, however, we do not yet have a low-order model for reliably predicting the dynamics of the LEV and its influence on the force generated by the wing. Such a model would be valuable, if not essential, for optimizing the wing structure and kinematics and for designing a flight control strategy for agile maneuvering of the vehicle. Current strategies for optimization and control rely on traditional quasi-steady models, constructed phenomenologically [4] or obtained experimentally by system identification [20]. Though such quasi-steady models can approximately account for the unsteady aerodynamic phenomena by, for example, utilizing the peak (or stroke-averaged) rather than steady-state forces, they cannot be used to exploit the LEV in a direct fashion, or for effecting maneuvers that occur on a timescale of a few wingbeats (as many airborne creatures are capable of).

Phenomenological approaches to low-order modeling of unsteady aerodynamics date from the work of 1920s and 1930s. At their heart, these models decompose the force and moment on the wing into contributions from circulatory (i.e., vortex-induced) and non-circulatory (i.e., inertial reaction or added mass) effects. The models are generally based on potential flow theory, in which the circulatory forces are accounted for by directly computing the influence of shed vorticity, whose dynamics are generally represented by some simplified description: as a sheet (e.g., the flat wake of Wagner [49], Theodorsen [46] and von Kármán and Sears [48], the similarity solution for spiral evolution by Pullin and Wang [39], or with full nonlinear dynamics by Nitsche and Krasny [26,34], Jones [22], Shukla and Eldredge [44] and Alben and Shelley [1]); a continuous sequence of point vortices [2,21,24]; or a limited number of point vortices with evolving strengths [5,8,18,29]. In all of these models, vorticity is generated at salient edges via a Kutta condition.

These potential flow models often do a fair job of predicting the circulatory force and moment on the wing when the angle of attack remains small and no LEV is generated. However, their success is less certain in flows in which the LEV plays a significant role, that is, when one might apply a Kutta condition at both the leading and trailing edges. The physics of the interaction between the developing LEV with the wing are, in many circumstances, essentially viscous, causing the inviscid model to develop unphysical behavior [44]. However, at sufficiently high angles of attack, the development and shedding of the LEV can be identified with an inviscid process, and a potential flow approach seems to provide adequate results [2,3].

The present work has two objectives. First, as in [2], we are interested in using an inviscid vortex model for predicting LEV flows, and particularly we seek to understand the range of circumstances under which the model is physically plausible. Secondly, in the interest of ensuring the model's viability for optimization and control, we wish for such an inviscid model to have as few degrees of freedom as possible. This second objective precludes any approach that attempts to capture the detailed dynamics of the shed vortex sheet, since such dynamics necessarily require tracking hundreds to thousands of computational elements. Thus, we are guided here by the work of Brown and Michael [5] and Edwards [11], who relied on two moving point vortices of time-varying strength to simulate the vortex sheets developing from the swept leading edges of a delta-wing aircraft. The stationary vortex model of Saffman and Sheffield [42] and vortex-sink combination of Rossow [41], Mourtos and Brooks [33], and Davis et al. [9] are formulated in a similar spirit, in the context of wing section aerodynamics. Another recent study by Pitt Ford and Babinsky has attempted to fit experimental data at large angle of attack to a stationary vortex model [36].

In the model presented here, point vortices are released from the salient edges of a flat plate, and their strengths are instantaneously determined at each instant by the Kutta condition at both edges. Their positions evolve according to, in our initial version of the model, the so-called Brown–Michael equation [5]. Then, when the strength of a vortex reaches an extremum, it is frozen at that value and the vortex subsequently moves according to the usual Kirchhoff velocity, and a new vortex is released from the corresponding edge. In fact, this model is actually inextricably bound to this 'shedding' criterion, for if the strength of a vortex is set constant at anything other than an extremum, then the discontinuous rate of change of this strength leads to a corresponding jump in the force predicted on the plate. Thus, it is not possible to use alternative shedding criteria, based on, for example, a formation number for the developing vortex [6,31].

In order to relax the shedding criterion, we present a model based on a generalization of one recently used by Tchieu and Leonard [45] for predicting the effect of control on a wing undergoing arbitrary small angle-of-attack motions. Those authors relied on a 'conservation of impulse' argument to arrive at an evolution equation for vortices of time-varying strength shed from the trailing edge of a flat plate. Though their discussion is brief, the model equation can be interpreted under the following principle: set the motion of a vortex so that any temporal variation of its strength has no direct effect on the force on the plate. We show here

that this is equivalent to ensuring that the rate of change of the associated impulse of the vortex is equal to that of a constant-strength 'surrogate' vortex of identical instantaneous position and strength, but moving with the usual Kirchhoff velocity. Tchieu and Leonard [45] found that the lift predicted with this approach agreed much better than a Brown–Michael model with the classical Wagner theory for impulsive change of angle of attack. The evolution equation we develop here, which we call the 'impulse matching model', is based on a generalization of this principle and is applied to vortices shed from both edges. It will be shown that the forces predicted by this new model are in better agreement with experimental and high-fidelity computational results than the Brown–Michael model.

We present both the Brown–Michael and the new model in Sect. 2 and contrast them with each other. The target problem of this study—the pitching and perching of a flat plate—is defined mathematically in Sect. 3. The results of the model, including comparison with experiments and high-fidelity computations, and a decomposition of the lift into inertial and circulatory contributions, are presented in Sect. 4. We also present an evaluation of results for a flat plate started impulsively at fixed angle of attack. Finally, some ongoing extensions of the model, for example, to finite aspect ratio wings, are discussed in Sect. 5.

2 Model formulation

We seek the fluid force and moment exerted on an infinitely thin flat plate in arbitrary motion in the presence of point vortices when the fluid is otherwise at rest. It is convenient to use complex potentials, so that the plate will be mapped from a circle in the $\zeta = \xi + i\eta$ plane via the Joukowski mapping, as depicted in Fig. 1.

We express the complex mapping for a plate of semi-chord length a as

$$z(\zeta) = z_c + \tilde{z}(\zeta)e^{i\alpha}, \tag{1}$$

where

$$\tilde{z}(\zeta) = \frac{a}{2}\left(\zeta + 1/\zeta\right). \tag{2}$$

The circle has unit radius in the ζ plane, that is, $\zeta = e^{i\theta}$ describes the surface, where $\theta \in [0, 2\pi)$. The leading edge is labeled as z_{10} and is identified with $\zeta = 1$ (i.e., $\tilde{z}_{10} = a$); the trailing edge is z_{20} and is mapped to $\zeta = -1$ ($\tilde{z}_{20} = -a$). The Jacobian of this mapping is

$$z'(\zeta) = \frac{a}{2}e^{i\alpha}\left(1 - 1/\zeta^2\right), \tag{3}$$

where $()'$ denotes the derivative with respect to the argument. For simplicity, we first consider a single vortex of strength Γ_v located at ζ_v in the circle plane; the result can easily be generalized to multiple vortices by linear superposition.

For a plate in arbitrary rigid body motion in the presence of a single vortex, the complex potential in the circle plane is (see [32])

$$\tilde{F}(\zeta) = -\frac{ia\tilde{V}}{\zeta} - \frac{i\Omega a^2}{4\zeta^2} + \frac{\Gamma_v}{2\pi i}\left[\log(\zeta - \zeta_v) - \log(\zeta - \zeta_v^{(i)})\right], \tag{4}$$
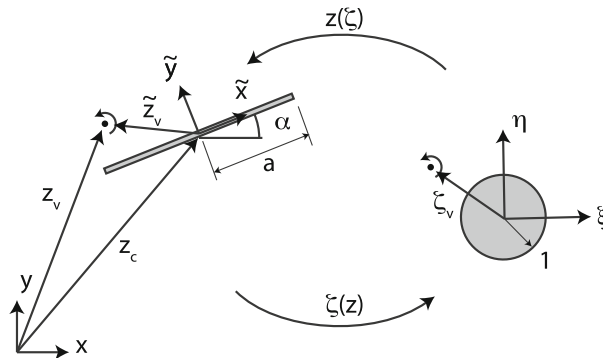

Fig. 1 Schematic of plate mapping to circular cylinder of unit radius in the ζ-plane

where $\zeta_v^{(i)} = 1/\zeta_v^*$ is the position of the image vortex (and $()^*$ denotes complex conjugate), and the leading dipole and quadrupole terms constitute rigid body modes. Here, $\dot{z}_c e^{-i\alpha} = \tilde{U} + i\tilde{V}$ is the complex velocity of the plate in its body-fixed coordinate system, and $\Omega = \dot{\alpha}$ is the angular velocity.

A point vortex of constant strength at position z_v will move with the Kirchhoff velocity (the local fluid velocity minus the vortex's self-contribution), denoted by W_{-v}:

$$\frac{dz_v}{dt} = W_{-v}^*(z_v) = \left[z'^*(\zeta_v)\right]^{-1} \lim_{\zeta \to \zeta_v} \left[\frac{\partial \tilde{F}}{\partial \zeta} - \frac{\Gamma_v}{2\pi i}\frac{1}{\zeta - \zeta_v} - \frac{\Gamma_v}{4\pi i}\frac{z''(\zeta)}{z'(\zeta)} \right]^*. \tag{5}$$

The final term inside brackets is the so-called Routh correction [7], which accounts for the curvature of the mapping.

2.1 Force on the plate

The force on the plate can be obtained from the linear impulse

$$F_x + iF_y = -\rho \frac{dP}{dt}, \tag{6}$$

where the impulse can be obtained from the general vector formula [14]

$$\boldsymbol{P} = \int_{A_f} \boldsymbol{x} \times \boldsymbol{\omega}\, dA + \oint_{S_b} \boldsymbol{x} \times \boldsymbol{\gamma}_\omega\, ds + \oint_{S_b} \boldsymbol{x} \times (\boldsymbol{\gamma}_b + \boldsymbol{n} \times \boldsymbol{u}_b)\, ds \tag{7}$$

where $\boldsymbol{\omega}$ is the ambient vorticity in the fluid region (denoted by A_f), $\boldsymbol{u}_b$ is the local surface velocity of the body with outward normal $\boldsymbol{n}$ on surface S_b, and $\boldsymbol{\gamma}_\omega$ and $\boldsymbol{\gamma}_b$ are the strengths of the vortex sheets that exist on the body surface in response to ambient vorticity and body motion, respectively. Similarly, the torque about the origin can be written in vector form in terms of angular impulse as

$$\boldsymbol{\tau}_0 = -\rho \frac{d\boldsymbol{\Pi}_0}{dt} \tag{8}$$

where the angular impulse about the origin can be written as

$$\boldsymbol{\Pi}_0 = \frac{1}{2}\int_{A_f} \boldsymbol{x} \times (\boldsymbol{x} \times \boldsymbol{\omega})\, dA + \frac{1}{2}\oint_{S_b} \boldsymbol{x} \times (\boldsymbol{x} \times \boldsymbol{\gamma}_\omega)\, ds + \frac{1}{2}\oint_{S_b} \boldsymbol{x} \times [\boldsymbol{x} \times (\boldsymbol{\gamma}_b + \boldsymbol{n} \times \boldsymbol{u}_b)]\, ds. \tag{9}$$

Finally, by Kelvin's circulation theorem,

$$\int_{A_f} \boldsymbol{\omega}\, dA + \oint_{S_b} \boldsymbol{\gamma}_\omega\, ds + \oint_{S_b} (\boldsymbol{\gamma}_b + \boldsymbol{n} \times \boldsymbol{u}_b)\, ds = 0. \tag{10}$$

Note that the sum of the surface terms in the integrands of these formulas is simply $\boldsymbol{\gamma}_\omega + \boldsymbol{\gamma}_b + \boldsymbol{n} \times \boldsymbol{u}_b = \boldsymbol{n} \times \boldsymbol{u}^+$, where $\boldsymbol{u}^+$ is the local fluid velocity adjacent to the body.

Expression (7) for impulse can be transformed into complex notation if we note that the unit normal vector (in the body-fixed coordinate system) can be expressed as $(\tilde{n}_x + i\tilde{n}_y)\, ds = -id\tilde{z}$. With some manipulation, it can be shown that the impulse components can be written as

$$P = P_x + iP_y = -e^{i\alpha}\left[i\Gamma_v \tilde{z}_v + \oint i\tilde{z}(\zeta)\mathrm{Re}\left(\frac{\partial \tilde{F}}{\partial \zeta}\, d\zeta\right) \right]. \tag{11}$$

This can be further manipulated by noting that the imaginary part of $(\partial \tilde{F}/\partial \zeta)d\zeta$ gives no contribution to a flat plate of infinitesimal thickness. (It can be shown that this actually contributes the impulse associated with the fluid displaced by the body [43].) Finally, after using residue theory to evaluate the integrals, we arrive at

$$\rho P = ie^{i\alpha}\left[\tilde{M}_{yy}\tilde{V} - \frac{1}{2}\rho a \Gamma_v(\zeta_v - \zeta_v^{(i)}) \right], \tag{12}$$

where $\tilde{M}_{yy} = \rho\pi a^2$ is the sole added-mass coefficient in the body-fixed frame. The first term gives rise to the inertial reaction force in response to linear accelerations and coupled rotations–translations of the plate. The second term represents the contribution from the vortex and its image (or alternatively, from the vortex, modified by the presence of the plate).

A similar procedure can be used to develop a complex expression for angular impulse about the centroid, $\Pi_c = \Pi_0 + \text{Im}(z_c^* P)$, by starting with the expression (9). We arrive at

$$\rho\Pi_c = I_{zz}\Omega + \frac{1}{8}\rho a^2 \Gamma_v \left[2 + \frac{1}{\zeta_v^{*2}} + \frac{1}{\zeta_v^2} - \left(\zeta_v + \frac{1}{\zeta_v} \right) \left(\zeta_v^* + \frac{1}{\zeta_v^*} \right) \right], \tag{13}$$

where $I_{zz} = \rho\pi a^4/8$. Finally, note that Kelvin's circulation theorem is automatically enforced by ensuring that the image vortex has equal and opposite strength of its partner.

2.2 Brown–Michael model

The Brown–Michael model is based on releasing and tracking a point vortex whose strength varies in time in order to satisfy, at each instant, the Kutta condition at the edge from which it was released. In potential flow, a point vortex with time-varying strength gives rise to a multi-valued pressure distribution, manifested in the time derivative of the velocity potential in the Bernoulli equation. Thus, in order to prevent a net force from acting on the vortex and associated branch cut (which can be imagined as extending from the vortex to its image through the releasing edge), Brown and Michael [5] and Edwards [11] showed independently that the vortex must evolve according to the modified equation

$$\frac{\mathrm{d}z_v}{\mathrm{d}t} + \frac{(z_v - z_{j0})}{\Gamma_v} \frac{\mathrm{d}\Gamma_v}{\mathrm{d}t} = W_{-v}^*(z_v), \tag{14}$$

where $j = 1$ or 2, depending on the releasing edge. This equation was originally constructed by adding a Kutta–Joukowski force, proportional to the difference in velocity between the vortex and surrounding fluid, in order to cancel out the unbalanced force on the vortex and branch cut. Michelin and Llewellyn Smith [29] recently formalized the original derivation by setting to zero the rate of change of momentum inside a contour just enclosing the vortex and the branch cut.

In the present context of a flat plate, a point vortex is released from each edge of the plate, and its position evolves by the modified advection Eq. (14). If the strength of the vortex reaches an extremum, this strength is frozen and the vortex continues to advect with the Kirchhoff velocity (5) (in this work, we describe this event as 'shedding', following [8] and [29].) The vortices' positions and strengths are denoted by $\{(z_j, \Gamma_j), j = 1, \ldots, N\}$. Thus, at any given instant, vortices 1 and 2 (released from edges z_{10} and z_{20}, respectively) have time-varying strength to satisfy a regularity condition at their respective edge, while any other vortex $j = 3, \ldots, N$ has constant strength. These regularity conditions can be shown to be

$$2\tilde{V}\zeta_{k0} + \Omega a + \sum_{j=1}^{N} \frac{\Gamma_j}{\pi a} \text{Re}\left(\frac{\zeta_j + \zeta_{k0}}{\zeta_j - \zeta_{k0}} \right) = 0, \quad k = 1, 2, \tag{15}$$

where $\zeta_{10} = 1$ and $\zeta_{20} = -1$. Equations (15) are solved for Γ_1 and Γ_2 at each instant, based on the instantaneous states of the plate and the constant-strength vortices.

2.3 Impulse matching model

As mentioned above, the Brown–Michael model is accompanied by a restrictive criterion for shedding, namely, that the vortex strength must reach an extremum before it can be frozen and allowed to evolve as a simple point vortex. Thus, it is desirable to loosen this criterion in order to provide more flexibility for model adaptation. The model developed by Tchieu and Leonard [45] is generalized here, based on the principle that any time variation of the strength of the point vortex should have no direct effect on the force. Since the force arises from the rate of change of impulse, then we achieve this principle as follows: We hypothesize a virtual 'surrogate' vortex at the same instantaneous location and with the same instantaneous strength, but which moves with constant strength at the Kirchhoff velocity (5). Then, the equation of motion for the actual vortex is derived

by setting the rate of change of its linear impulse to that of the constant-strength surrogate. In other words, the vortex is set in motion in such a way that it cancels the effect of $d\Gamma_v/dt$ on the force on the body.

It is important to note that this approach ensures that the force on the body is continuous in time when the strength of the vortex is frozen, regardless of whether this strength has reached an extremum; the variable-strength vortex is merely replaced by its constant-strength surrogate, with no effect on the impulse or its rate of change. Indeed, this is the *only* approach that will ensure this behavior. Thus, it allows us to use alternative criteria for freezing the strength and releasing a new vortex, for example, based on a formation number or from empirical results. In this work, which focuses only on early-stage development of the LEV, we retain the extremum criterion. The strengths of the two developing point vortices are determined by applying the Kutta condition at each edge, as in the Brown–Michael model.

Let us label the position and strength of this constant-strength surrogate vortex as z_v^{CS} (or ζ_v^{CS} in the circle plane) and Γ_v^{CS}, respectively. Then, by construction,

$$\frac{dz_v^{CS}}{dt} = W_{-v}^*(z_v^{CS}), \qquad \frac{d\Gamma_v^{CS}}{dt} = 0, \tag{16}$$

and at any instant t_0, $z_v^{CS}(t_0) = z_v(t_0)$ (and $\zeta_v^{CS}(t_0) = \zeta_v(t_0)$) and $\Gamma_v^{CS} = \Gamma_v(t_0)$. The principle of the model is expressed mathematically as

$$\frac{dP}{dt}(t_0) = \frac{dP^{CS}}{dt}(t_0). \tag{17}$$

Since the body motions are identical for the vortex and its constant-strength surrogate, this equation reduces to

$$\frac{d}{dt}(\zeta_v - \zeta_v^{(i)}) + \frac{(\zeta_v - \zeta_v^{(i)})}{\Gamma_v}\frac{d\Gamma_v}{dt} = \frac{d}{dt}(\zeta_v^{CS} - \zeta_v^{CS(i)}). \tag{18}$$

Thus, it remains to transform this equation into the z (physical) domain. In the Appendix, it is shown that this results in the following equation of motion for the vortex:

$$\frac{dz_v}{dt} + \frac{h(z_v - z_{10}, z_v - z_{20})}{\Gamma_v}\frac{d\Gamma_v}{dt} = W_{-v}^*(z_v), \tag{19}$$

where

$$h(v, w) = \frac{|v|w + |w|v}{|v| + |w|}. \tag{20}$$

It is noted that the model derived here is specific to the geometry—in this case, a flat plate of finite length. This is not the case for the Brown–Michael model. However, the basic principle of impulse matching can be extended to other geometries, such as the semi-infinite flat plate considered by Pullin [38].

2.3.1 Special case of Tchieu and Leonard

Note that we can recover the special case presented by Tchieu and Leonard [45] by limiting shedding to the trailing edge and restricting the shed vortex to a planar wake on the x axis and forcing its constant-strength surrogate to move at the free-stream velocity, U_∞ (in a frame fixed to the plate):

$$z_v \to x_v, \qquad W_{-v}^*(z_v) \to U_\infty. \tag{21}$$

Then, with the plate oriented with small angle relative to the free stream, $z_{10} \approx -a$ and $z_{20} \approx a$, and the model simplifies to

$$\frac{dx_v}{dt} + \frac{(x_v^2 - a^2)}{x_v \Gamma_v}\frac{d\Gamma_v}{dt} = U_\infty, \tag{22}$$

which is identical to the model presented in [45].

2.3.2 Comparison with Brown–Michael model

Finally, it is useful to contrast the present model with the Brown–Michael equation (14), for which we can define $h^{BM}(v, w) = \{v, w\}$, where the selection between v and w is determined by the edge from which the vortex was shed. Indeed, using the approach taken by Michelin and Llewellyn Smith [29], it can be shown that the difference between h and h^{BM} is proportional to the spurious force, F^{bc}, that develops on the branch cut and vortex using the present model:

$$F^{bc} = \mathrm{i}\rho \frac{\mathrm{d}\Gamma_v}{\mathrm{d}t}(h^{BM} - h). \tag{23}$$

One can interpret this as the external force one must apply in order for the vortex to move with a velocity other than that dictated by the Brown–Michael equation. For a vortex released from the leading edge, z_{10}, for example,

$$h^{BM} - h = -2a\mathrm{e}^{\mathrm{i}\alpha} \frac{|z_v - z_{10}|}{|z_v - z_{10}| + |z_v - z_{20}|}. \tag{24}$$

Thus, the difference becomes negligibly small when the vortex is near the releasing edge. When the vortex has moved far from the plate, $|z_v - z_c| \gg a$, then $h \approx z_v - z_c$, and therefore $h^{BM} - h \approx -a\mathrm{e}^{\mathrm{i}\alpha}$. However, the strength of the vortex is nearly invariant (or set constant) at such large distances, which renders the spurious force negligibly small. So in most cases, the fact that an external force must be applied is of little concern.

2.4 Small-time behavior

Just after a vortex is released from an edge, the evolution equations are nearly singular and therefore it is more convenient to solve them analytically for a short interval. We define the relative position η_j by the relation $\zeta_j = \zeta_{j0}(1 + \eta_j)$ and assume that $|\eta_j| \ll 1$. This procedure follows the one used by Cortelezzi and Leonard [8] and Michelin and Llewellyn Smith [29] for the Brown–Michael model. Here, we present it for both the Brown–Michael and the new impulse matching model, and distinguish the two with the parameter κ, which takes the values 0 and 1, respectively.

Using the generalized evolution equation (19) and the regularity condition (15), and assuming that the flow is otherwise irrotational (i.e., soon after initiating the motion of the plate from rest), it can be shown that, after short interval Δt, the vortex position in the circle plane is

$$\eta_j(\Delta t) = \frac{C|\hat{V}_j|^{1/3}}{2^{1/2}a^{2/3}(2\mu + 1)^{1/3}} \mathrm{e}^{\mathrm{i}\zeta_{j0}\mathrm{sgn}(V_j)\tilde{\phi}} \Delta t^{(\mu+1)/3}, \tag{25}$$

where

$$\tilde{\phi} = \arcsin\left(\frac{1}{2^{1/2}C^3}\right), \qquad C = \left[\frac{1 + 2\mu + \kappa(1 + 4\mu)/6}{1 + 2\mu + \kappa(1 + 4\mu)/3}\right]^{1/6}. \tag{26}$$

The parameter V_j denotes the fluid velocity induced by body motion, evaluated in the circle plane at positions tangent to the mapped plate edges (i.e., at ζ_{j0}); here, $V_j = -a\tilde{V} - \zeta_{j0}\Omega a^2/2$. The body motion, and hence V_j, is assumed to follow a power law, $V_j = \hat{V}_j t^\mu$, where $\hat{V}_j$ and μ are determined by the dominant component of the initial motion.

The circulation associated with this initial development of the vortex is given by the expression

$$\Gamma_j = \zeta_{j0}\mathrm{sgn}(V_j) \frac{\pi|\hat{V}_j|^{4/3}}{a^{2/3}(2\mu + 1)^{1/3}} \left[1 + \frac{\kappa}{6}\left(\frac{1 + 4\mu}{1 + 2\mu}\right)\right]^{1/2} \Delta t^{(4\mu+1)/3} \tag{27}$$

For the Brown–Michael case, $\kappa = 0$, the expressions (25) and (27) revert to those given in [8]. It is noted that, in deriving these results, we have not presumed that the flow is self-similar at early times, as it is for a semi-infinite plate [38]. As a consequence, the length scale a imposed by the plate enters the results even at early times.

The impulse required to generate this motion from rest is provided by the expression (12). It is straightforward to show, using the results obtained thus far for small-time behavior, that

$$\rho P = \mathrm{i}\mathrm{e}^{\mathrm{i}\alpha} \left[\tilde{M}_{yy} \left(1 + |\eta_1|^2 + |\eta_2|^2 \right) \tilde{V} + \rho(\pi a^3/2) \left(|\eta_1|^2 - |\eta_2|^2 \right) \Omega \right]. \qquad (28)$$

Thus, the vortices shed from both edges supplement the inherent added mass of the plate, whereas the body rotation only contributes if there is asymmetry between the two edges (for example, if the pitch axis is off of the centroid).

2.5 High-fidelity simulations

The high-fidelity computations in this study are performed with the viscous vortex particle method (VVPM), in which the Navier–Stokes equations are discretized by vorticity-bearing particles that advect with the local fluid velocity. The method uses a fractional stepping procedure, in which the fluid convection, fluid diffusion, and vorticity creation are treated in separate substeps of each time increment. The details of the VVPM algorithm can be found in [13].

3 Problem statement

The pitching wing to be studied in this work is drawn schematically in Fig. 2. A two-dimensional wing profile of chord $c = 2a$, thickness $0.023c$, and semicircular edges translates rectilinearly at speed $U(t)$ in an incompressible flow with density ρ and kinematic viscosity ν. In the low-order model of this problem, the plate is approximated as an infinitely thin flat plate with sharp edges. The wing undergoes a pitch-up maneuver at nominal angular velocity $\dot{\alpha}_0$ to $90°$ about an axis situated X_p aft of the leading edge. Two classes of translational motion are considered here: *pitching*, in which $U(t) = U_0$, a constant speed, and *perching*, as defined by Granlund et al. [19], in which the wing starts at speed U_0 and decelerates linearly to rest during the pitch-up interval.

The angle of attack, α, is prescribed over time with a schedule given by

$$\alpha(t) = \alpha_0 \frac{G(t)}{\max G}, \qquad (29)$$

where the maximum of G is taken over the time interval of interest, so that the maximum angle α_0 is achieved when G reaches this maximum. This function G describes a smoothed pitch-up maneuver starting at zero angle,

$$G(t) = \log \left[\frac{\cosh(a_s U_0(t - t_1)/c)}{\cosh(a_s U_0(t - t_2)/c)} \right] - a_s U_0(t_1 - t_2)/c. \qquad (30)$$

The parameter a_s controls the speed of the transitions between kinematic intervals, with larger values producing sharper transitions. The times t_1 and t_2 represent transition instants during the maneuver: t_1 is the start of the pitch-up (and start of the deceleration for the perching maneuver) and $t_2 = t_1 + \alpha_0/\dot{\alpha}_0$ is the end of the pitch-up (and the end of the deceleration in perching). For the cases studied here, the pitch-up starts at $t_1 = c/U_0$, which allows sufficient time for boundary layers to develop on the plate prior to the initiation of rotation. (Note that, for the function G to work as designed, the aforementioned maximum of G should be taken over a time interval $[t_1, t_b]$, where $t_b \geq t_2$. Clearly, this maximum is simply $G(t_b)$ for the function specified here, and if $t_b \gtrsim t_2 + 2c/(a_s U_0)$, then $\max G \approx 2a_s U_0(t_2 - t_1)/c$.)
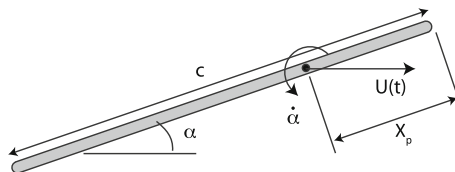

Fig. 2 Schematic of pitching wing

For purposes of the low-order models presented in Sect. 2, it is useful to note that, in the plate motion considered here, the $\tilde{y}$-velocity component in the plate-fixed coordinate system is given by $\tilde{V} = \Omega(X_p - c/2) - U \sin \alpha$, where $\Omega = \dot{\alpha}$.

The Reynolds number, $Re = U_0 c/\nu$, is fixed at 1,000 for all high-fidelity simulations; this choice is a compromise between ensuring sufficiently small effect from viscosity and requiring modest computational resources for full resolution of flow phenomena. The nominal pitch rate, $\dot{\alpha}_0$, is specified via the dimensionless parameter $K = \dot{\alpha}_0 c/(2U_0)$. The pitch axis is located throughout at the leading edge of the plate ($X_p = 0$), and the maximum angle α_0 is $\pi/2$. The smoothing parameter, a_s, in the kinematics described in (30) is set to 6 in all cases. The resulting lift and drag are scaled conventionally by $\rho U_0^2 c/2$ to form coefficients C_l and C_d, respectively. (Note that, in perching cases, the initial velocity is used for scaling the forces.)

The high-fidelity simulations are conducted throughout this study with particle spacing $\Delta x = 0.0025c$, time-step size $\Delta t = 0.0025c/U_0$, and 1,588 panels on the plate. The results were verified to be sufficiently converged with this choice of parameters.

4 Results

In this section, we report the results of applying both inviscid models to the pitching and perching problems, as well as to a problem involving impulsive translation of the plate at fixed angle of attack. We compare the results to the high-fidelity VVPM simulations and, where possible, the experimental results of Granlund et al. [19].

4.1 Pitching motion

4.1.1 Pitch rate $K = 0.2$

The lift and drag generated by the flat plate are shown in Fig. 3, and compared with the results of high-fidelity simulation (at Reynolds number 1,000) and the experiment (carried out at Reynolds number 20,000). The latter two results agree very well, which provides evidence that the forces are relatively insensitive to Reynolds number in this laminar/transitional regime. Both reduced models predict the trends of the force quite well with only six degrees of freedom (the strength and two coordinates for each vortex); in contrast, the numerical simulations ultimately use on the order of 5×10^5 computational particles, each with three degrees of freedom. The lift from all methods exhibits a rapid initial rise due to inertial reaction (as demonstrated below), reaches a maximum at around 40° angle of attack and then drops steadily toward zero as the wing becomes vertically oriented. The drag increases steadily with angle of attack, as one would expect, but drops quickly at the end of the interval due to
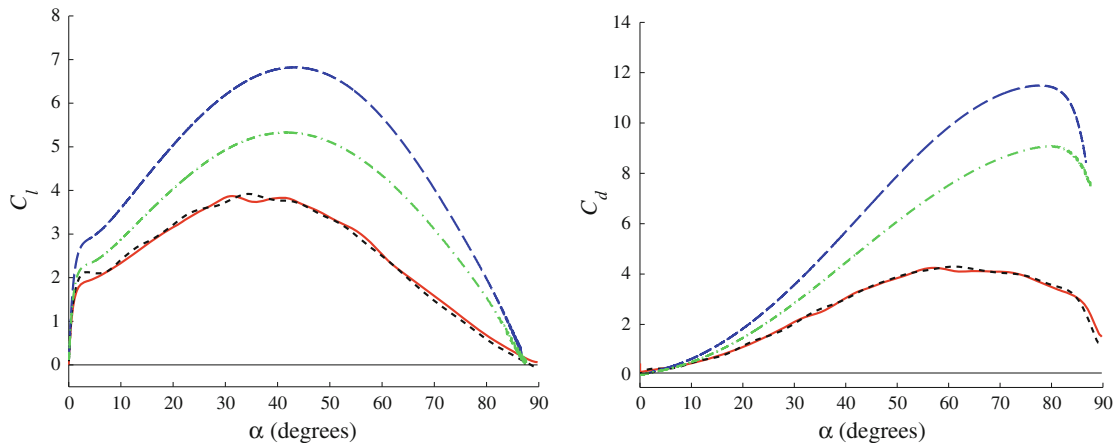

Fig. 3 Lift (*left*) and drag (*right*) coefficients for pitching motion at $K = 0.2$. Impulse matching model (*green dashed line*); Brown–Michael model (*blue dashed line*); VVPM simulation (*red solid line*); Experiment [19] (*black solid dashed line*) (Color figure online)
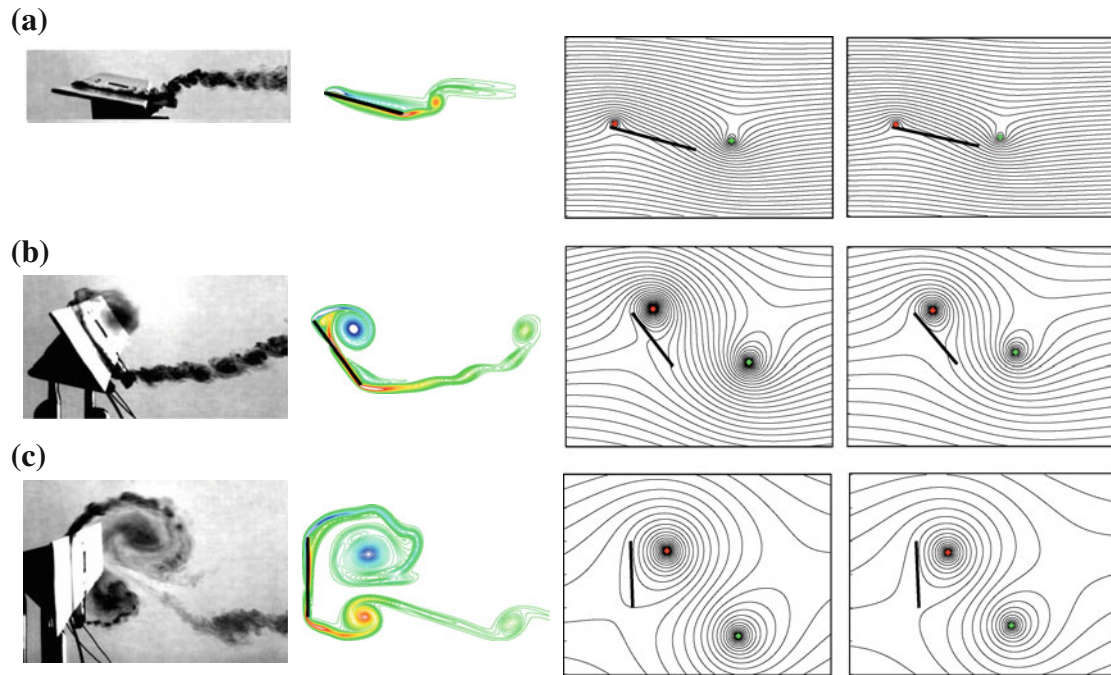
Fig. 4 Flow field of pitching motion for $K = 0.2$ at **a** $\alpha = 15°$, **b** $53°$ and **c** $90°$. *First column* dye visualization from experiments [19]; *second column* vorticity field of VVPM simulation; *third and fourth columns* streamlines in steadily translating frame from Brown–Michael and impulse matching models, respectively, with point vortex locations denoted with *colored circles* (Color figure online)

inertial reaction from the rapid deceleration of the pitching. Both models over-predict the force components; nevertheless, the impulse matching model performs consistently better than the Brown–Michael model.

Figure 4 depicts the flow field at $\alpha = 15°$, $53°$ and $90°$ during the pitching motion. By looking at the left two columns, one can clearly see that the flow fields from experiment and high-fidelity simulation are very similar to each other, aside from the shear instability in the higher Reynolds number experimental results. A starting vortex at the trailing edge is generated at the onset of rotation, and a leading-edge vortex develops during the ensuing pitch-up. This LEV remains relatively close to the suction side of the plate throughout the interval, and sits alongside a new trailing-edge vortex when the plate is vertical. The flow fields of the two low-order models—denoted by instantaneous streamlines—are presented in the right two columns (shown as mirror images of the actual models, in which the plates actually translate to the right); the differences between these models are difficult to detect. Most coherent structures in the experiments and computations are represented by a corresponding point vortex in the low-order model. However, the vorticity shed from the trailing edge is spread over an extended shear layer, so the point vortex represents this flow only approximately.

4.1.2 Pitch rate $K = 0.7$

Figure 5 depicts the lift and drag at a pitch rate of $K = 0.7$, and compares the results from both models with the high-fidelity VVPM simulations. (There are no experimental results available at this higher pitch rate.) As with the $K = 0.2$ case, both models capture the qualitative behavior of the force components quite well: the early inertial reaction force, followed by the peak and rapid decay of the lift, and the gradual rise and rapid decay of the drag. The quantitative agreement with the high-fidelity simulations is much better in this case, particularly for the impulse matching model.

The flow field depicted in Fig. 6 shows that, at this higher pitch rate, the vortex generated at the trailing edge is more coherent and, consequently, is better represented by a point vortex in the low-order model. (Note that only the Brown–Michael model results are shown here; the impulse matching model is very similar.) The shear instabilities developed near the edge of the maneuver are not captured by the models, of course, but these have little effect on the force generated by the plate.
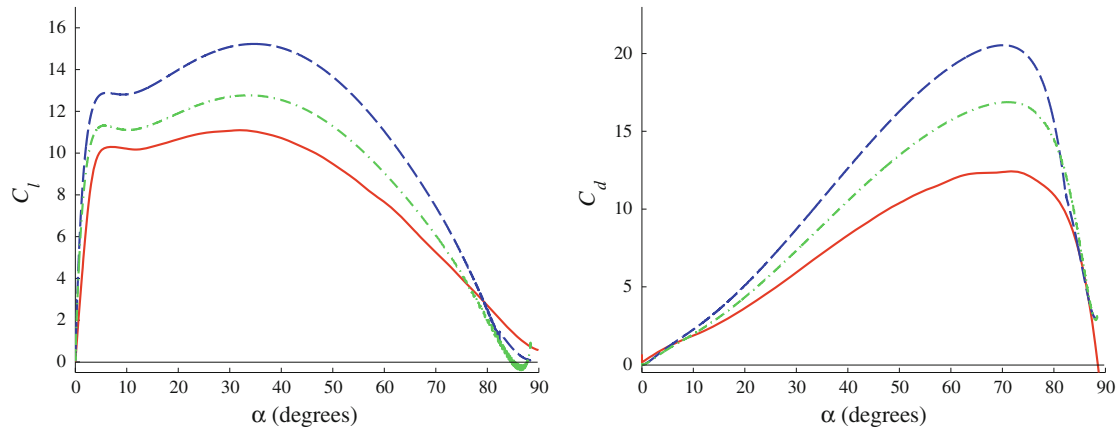
Fig. 5 Lift (*left*) and drag (*right*) coefficients between models for pitching motion at $K = 0.7$. Impulse matching model (*green dashed line*); Brown–Michael model (*blue dashed line*); VVPM simulation (*red solid line*) (Color figure online)
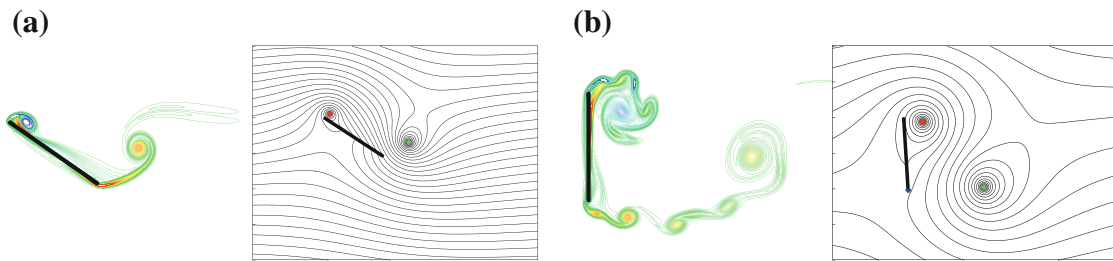

Fig. 6 Flow field of pitching motion for $K = 0.7$ at **a** $\alpha = 33°$ and **b** $90°$. *First image* in each pair: vorticity field of VVPM simulation; *second image*: streamlines from Brown–Michael model, with point vortex locations denoted with *colored circles* (Color figure online)

4.1.3 Decomposition of lift

In order to better understand the roles of inertial reaction and circulatory components in the lift generation, the lift obtained from the impulse matching model is decomposed in the left panels of Figs. 7 and 8 for the pitch rates $K = 0.2$ and $K = 0.7$, respectively. The inertial reaction arises from the first term of Eq. (12), and the circulatory component is defined by the remaining terms. In the inertial reaction at both pitch rates, the effect of the rapid acceleration of pitching is apparent in the early peak. The remainder of this component is associated with the coupled rotation and translation of the plate. As expected, the inertial reaction force is comparatively smaller at the lower pitch rate. The circulatory component, in both cases, exhibits a relatively simple dependence on the angle of attack, nearly symmetric about $45°$ and approximately zero at $0°$ and $90°$. This component generally provides a more important contribution to the overall lift, though its relative contribution is weaker with increasing pitch rate.

In order to provide a different perspective on the circulatory component of lift, the right panels of Figs. 7 and 8 exhibit the separate linear contributions of each vortex (and its image) to the impulse at the two respective pitch rates. It is interesting to note that the trailing-edge vortex contributes most to the lift, and in fact, the leading-edge vortex apparently makes a largely negative contribution. This behavior is seemingly paradoxical in view of the significant pressure trough on the suction surface that is usually observed under the LEV (see, e.g., [47]). However, it is important to note that pressure is not directly related to the rate of change of impulse associated with any one vortex, and clearly does not admit a linear decomposition of the separate vortex effects, as impulse does. This can be understood in a different manner by noting that the LEV has an important indirect effect on the total impulse through its influence on the motion of the trailing-edge vortex. Indeed, if we suppress the shedding of a vortex from the leading edge in the model then we obtain the circulatory component of lift exhibited in Fig. 9. During the first half of the pitch-up, the lift is actually smaller when the LEV is suppressed; during the second half, the lift continues to rise, as the flow on the suction side remains attached in an unrealistic manner throughout the pitch-up in this potential flow model.
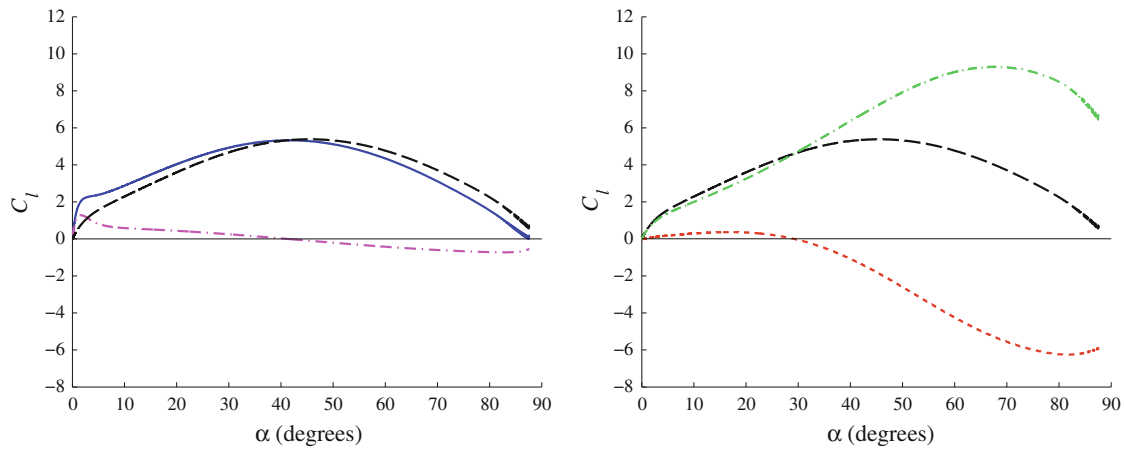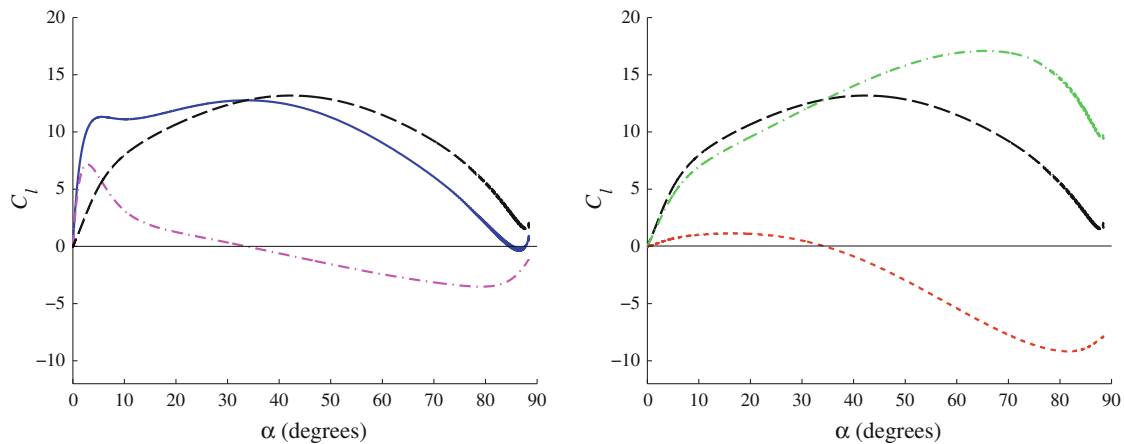
Fig. 7 (*Left*) Decomposition of lift from impulse matching model at $K = 0.2$ pitching motion. Circulatory component (*black dashed line*); inertial reaction component (*pink dashed line*); total lift (*blue dashed line*). (*Right*) Decomposition of circulatory component of lift into contributions from impulse of each vortex. Leading-edge vortex (*red solid dashed line*); trailing-edge vortex (*green dashed line*); total circulatory component from model (*black dashed line*) (Color figure online)

Fig. 8 (*Left*) Decomposition of lift from impulse matching model at $K = 0.7$ pitching motion. Circulatory component (*black dashed line*); inertial reaction component (*pink dashed line*); total lift (*blue dashed line*). (*Right*) Decomposition of circulatory component of lift into contributions from impulse of each vortex. Leading-edge vortex (*red solid dashed line*); trailing-edge vortex (*green dashed line*); total circulatory component from model (*black dashed line*) (Color figure online)

4.2 Perching motion

As described in the problem statement, perching differs from pitching only in that, in the former, the plate decelerates linearly to rest during the pitch-up. This maneuver is loosely inspired by the landing behavior of birds. The same pitch rates are considered here as in the pitching motion.

Figure 10 compares the lift and drag components between experiment, high-fidelity computation and the two models at $K = 0.2$ and 0.7, respectively. As in the pitching case, the high-fidelity simulation agrees well with the experiment (at $K = 0.2$, the only case with experimental data available). The models capture the qualitative behavior well, including the peak and long subsequent decay of lift, and the peak and decay of the drag. Both models over-predict the forces, but significantly less so than in the pitching case. Indeed, for the $K = 0.7$ case, the impulse matching model predicts the lift very well.

Note that, at large angles, the drag actually becomes negative, indicating a net thrust on the plate for a short interval of time. This is due to the combined influence of the sudden rotational deceleration and the steady deceleration of translation, both of which contribute added inertial forces in the direction of forward motion. In the pitching cases in Figs. 3 and 5, only the effect of quick rotational deceleration was present, and so the drag exhibited the same sudden decrease but was less prone to become negative.
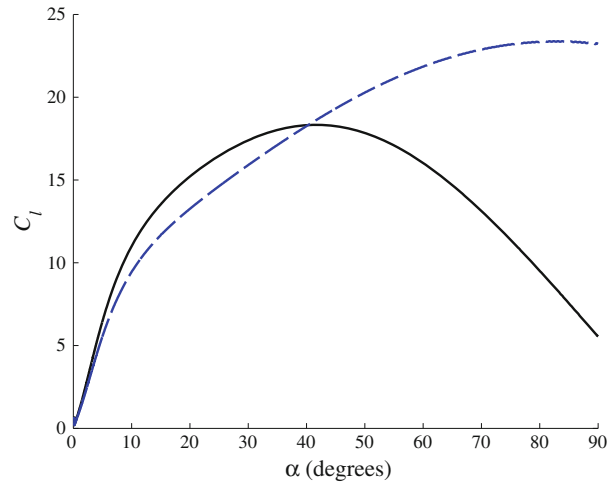
Fig. 9 Circulatory component of lift from pitching at $K = 0.7$, obtained from impulse matching model. Vortices shed from both edges (*black dashed line*); vortex shedding suppressed from leading edge (*blue dashed line*) (Color figure online)
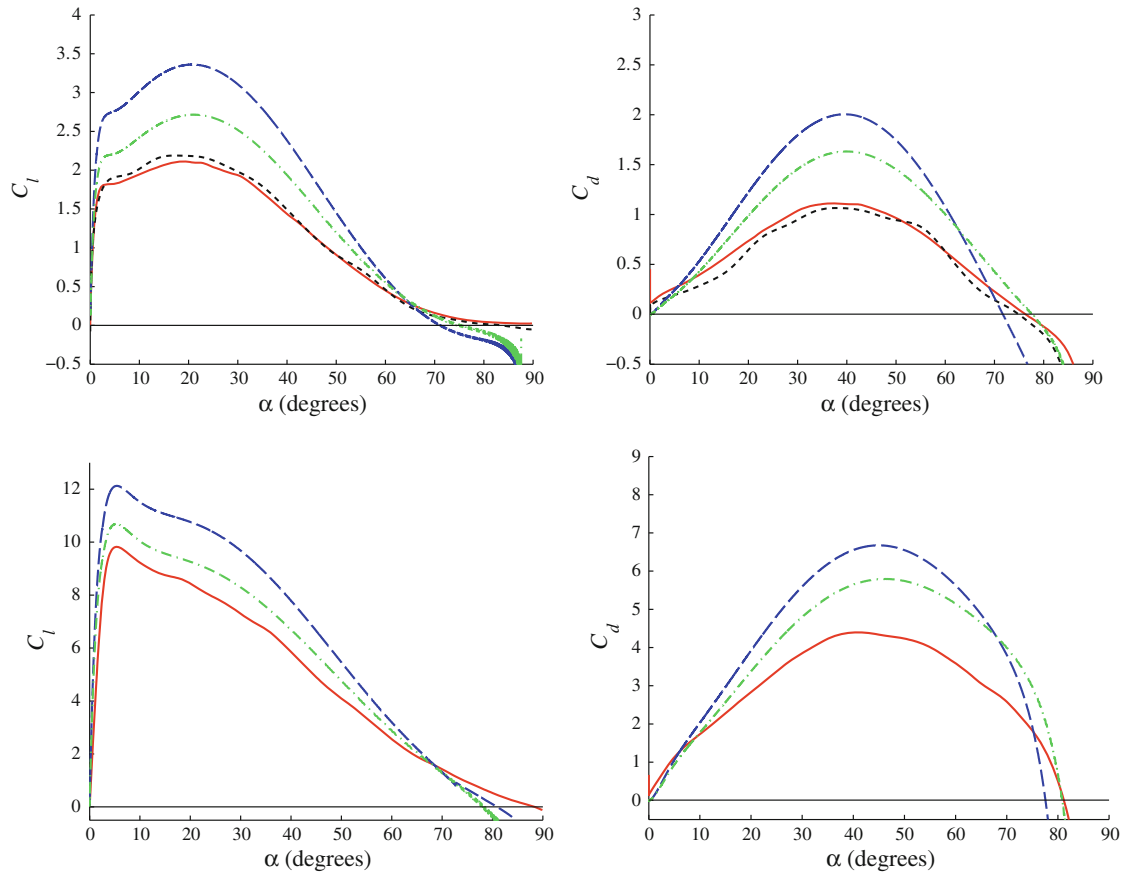

Fig. 10 Lift (*left*) and drag (*right*) coefficients for perching motion at $K = 0.2$ (*top*) and $K = 0.7$ (*bottom*). Impulse matching model (*green dashed line*); Brown–Michael model (*blue dashed line*); VVPM simulation (*red dashed line*); Experiment [19] (*black solid dashed line*) (Color figure online)

The flow fields for these two pitch rates are depicted in Figs. 11 and 12, respectively. For $K = 0.2$ and decreasing forward velocity, the size of the LEV is smaller and no shear instability is triggered compared with the pitching case in Fig. 4. Late in the interval, the model exhibits a second vortex shed from the leading edge
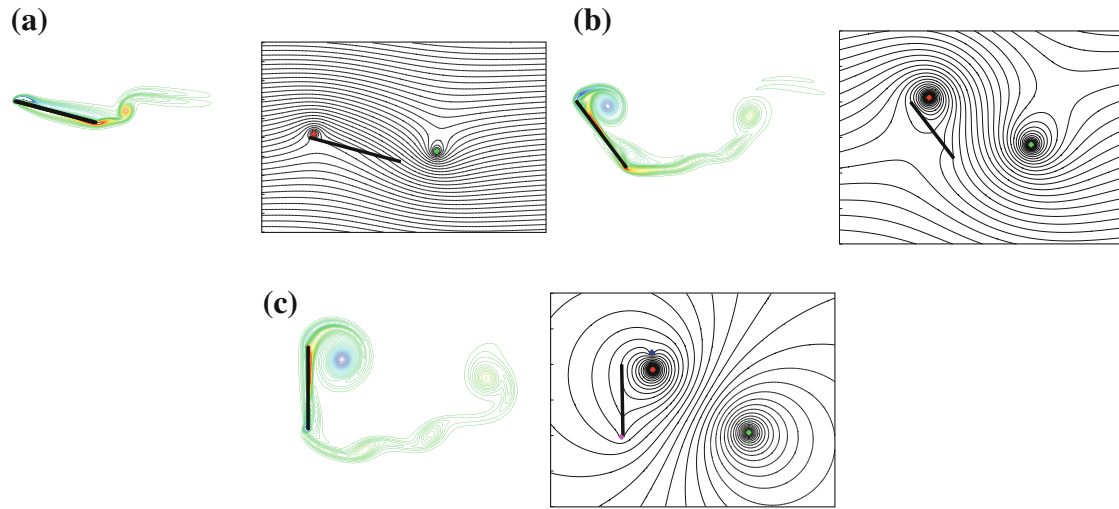
Fig. 11 Flow field of perching motion for $K = 0.2$ at **a** $\alpha = 15°$, **b** $53°$ and **c** $90°$. *First image* in each pair: vorticity field of VVPM simulation; *second image* streamlines from Brown–Michael model, with point vortex locations denoted with *colored circles* (Color figure online)
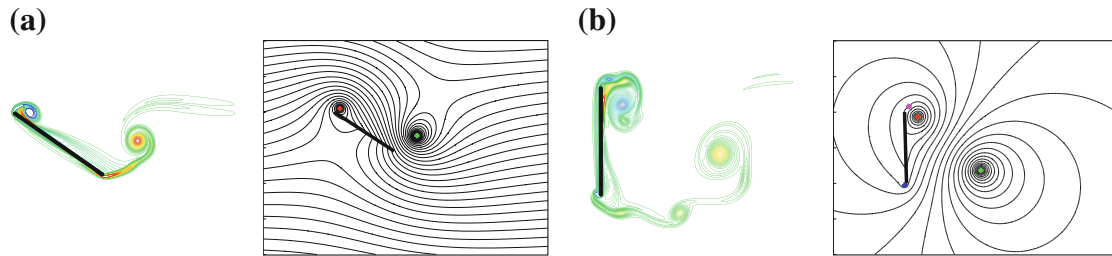

Fig. 12 Flow field of perching motion for $K = 0.7$ at **a** $\alpha = 33°$ and **b** $90°$. *First image* in each pair: vorticity field of VVPM simulation; *second image* streamlines from Brown–Michael model, with point vortex locations denoted with *colored circles* (Color figure online)

due to the deceleration of the plate, a behavior not seen in the pure pitching maneuver. Furthermore, a second vortex is shed from the trailing edge at the very end of the maneuver; the beginning of a similar vortex is apparent in the high-fidelity results.

For completeness, the same decomposition of the lift performed for the pitching motion is also performed here, and the results are exhibited in Figs. 13 and 14 for pitch rates $K = 0.2$ and 0.7, respectively. The inertial reaction and circulatory components are somewhat different here in the late stages of the maneuver, due to the linear deceleration of the plate. Otherwise, the behaviors are similar to the pitching case.

4.3 Impulsive translation at fixed angle of attack

In the previous two sections, the performance of the models was assessed on problems in which the aerodynamic force consists of both inertial and circulatory contributions, and the leading-edge vortex develops in response to both translation and rotation relative to the surrounding fluid. In this section, we explore the model performance in the simpler condition of impulsive translation at fixed angle of attack at Reynolds number 1,000. This motion generates an infinitely large inertial reaction force at $t = 0^+$, but at all subsequent times the force is due almost entirely to circulatory effects (with the exception of drag at small angles, which is dominated by skin friction). We evaluate both low-order models on this problem at three different fixed angles: $10°$, $45°$ and $90°$.

The results at the lowest angle, $10°$, are depicted in Figs. 15 and 16. Figure 15 presents a visual comparison of the vorticity contours from the VVPM results at three different instants with the streamlines (in the body-fixed frame) from the impulse matching model at the same instants. Note that the separation streamline
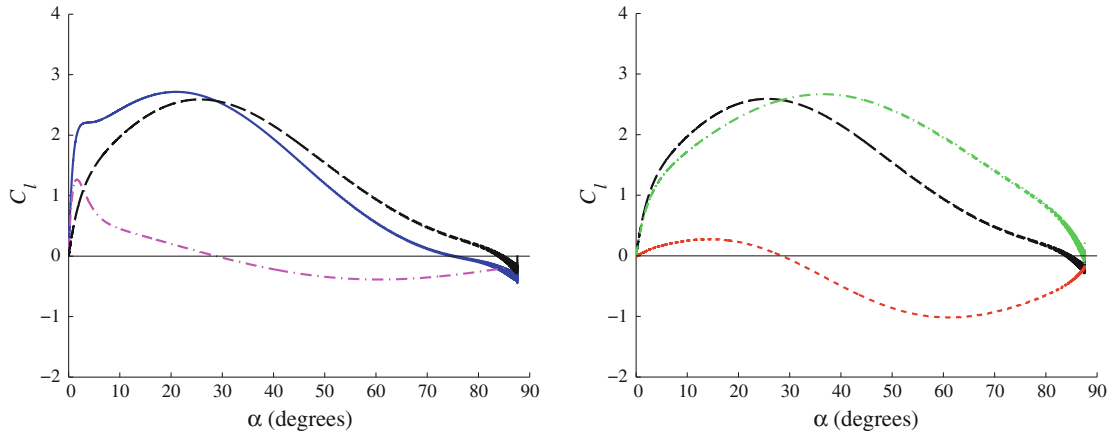
Fig. 13 (*Left*) Decomposition of lift from impulse matching model at $K = 0.2$ perching motion. Circulatory component (*black dashed line*); inertial reaction component (*pink dashed line*); total lift (*blue dashed line*). (*Right*) Decomposition of circulatory component of lift into contributions from impulse of each vortex. Leading-edge vortex (*red solid dashed line*); trailing-edge vortex (*green dashed line*); total circulatory component from model (*black dashed line*) (Color figure online)
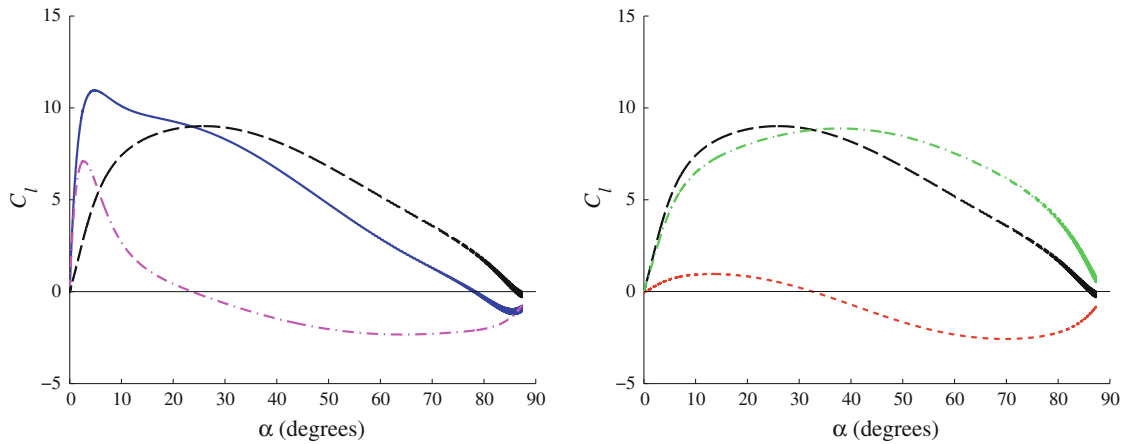

Fig. 14 (*Left*) Decomposition of lift from impulse matching model at $K = 0.7$ perching motion. Circulatory component (*black dashed line*); inertial reaction component (*pink dashed line*); total lift (*blue dashed line*). (*Right*) Decomposition of circulatory component of lift into contributions from impulse of each vortex. Leading-edge vortex (*red solid dashed line*); trailing-edge vortex (*green dashed line*); total circulatory component from model (*black dashed line*) (Color figure online)

is also included with the VVPM vorticity contours. At such a small angle, the separated flow does not deviate far from the upper surface of the plate, and consequently the leading-edge vortex is distributed over a large percentage of the chord. This behavior cannot be captured with a single point vortex, and thus the separation streamline predicted by the model is much more compact.

The force components predicted by the VVPM simulation and by the model are compared in Fig. 16. As was the case with the pitching and perching problems, both models capture the lift history qualitatively well but over-predict the magnitude, with the impulse matching model exhibiting closer agreement. Also shown in the lift history is a comparison with

$$C_L = 2\pi \sin \alpha \, \Phi(2U_0 t/c) \tag{31}$$

where Φ is the Wagner function [49], which accounts for vorticity shed from the trailing edge, but ignores contribution from the leading edge. The close agreement between this formula and the VVPM results confirms that the leading-edge vortex plays little role in force generation in this problem. The drag predicted by the models does not agree well with the VVPM results. However, this disagreement is significantly alleviated by augmenting the predicted drag from the impulse matching model with an approximate viscous contribution from the unsteady development of boundary layers on either side of the plate, obtained from solution of Stokes' first problem:
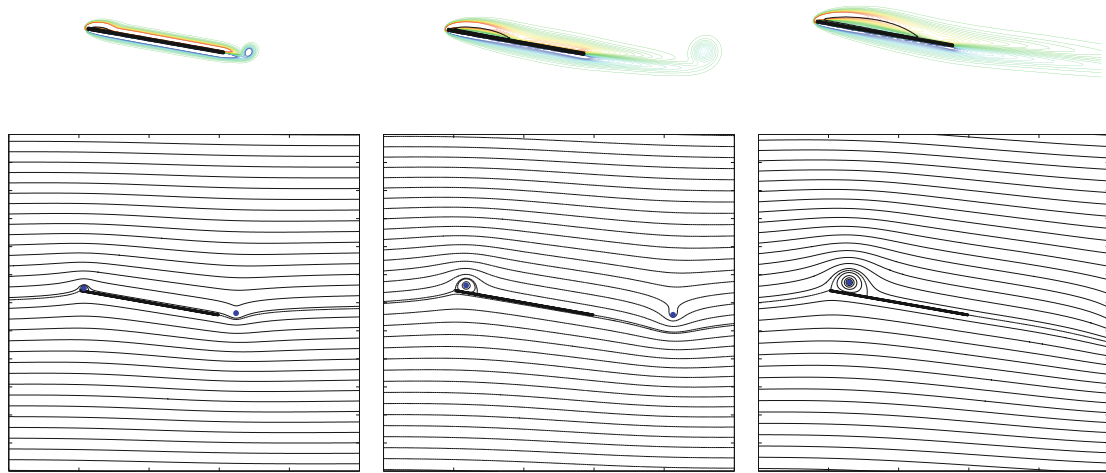
Fig. 15 VVPM vorticity contours (*first row*) and impulse matching model streamlines and point vortex locations (*second row*) for impulsive motion of flat plate at 10° angle of attack. The stagnation streamline is also shown in the VVPM results. *First column*: $Ut/c = 0.24$; *second column $Ut/c = 1$; third column $Ut/c = 2$*
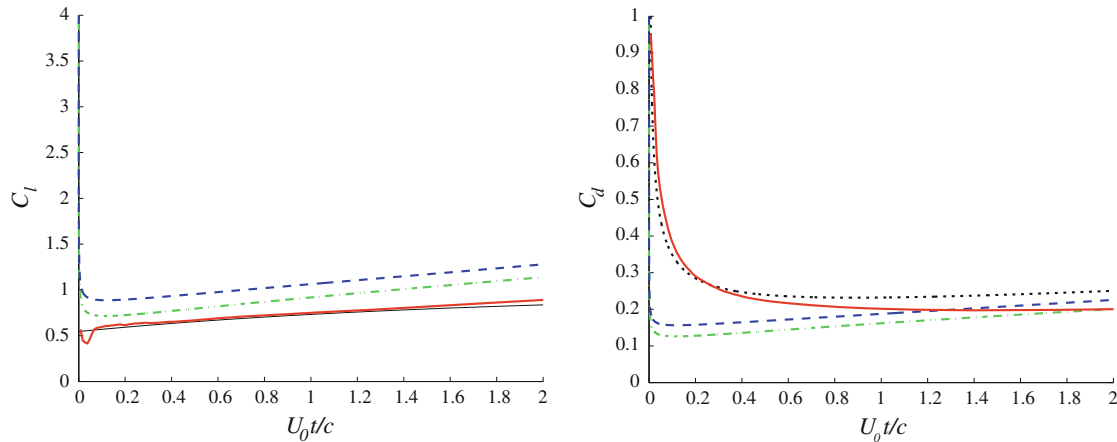

Fig. 16 Lift (*left*) and drag (*right*) coefficients for impulsive motion of flat plate at 10° angle of attack. Impulse matching model (*green dashed line*); impulse matching model with added viscous contribution (*black dotted line*); Brown–Michael model (*blue dashed line*); VVPM simulation (*red dashed line*); Wagner function (*black dashed line*) (Color figure online)

$$C_{D,v} = \frac{4}{\sqrt{\pi Re U_0 t/c}} \cos \alpha. \tag{32}$$

This viscous formula is only valid while the thickness of the boundary layer is much smaller than the chord length, so likely for less than a chord length of travel.

Figure 17 shows the flow field at three instants at 45 degrees angle of attack. At this large angle, the leading-edge vortex is significantly more coherent than at the lower angle of attack. For $U_0 t/c \lesssim 1$, the location of the leading-edge vortex predicted by the impulse matching model agrees visually with its position in the high-fidelity results; this agreement deteriorates as the vortex is prone to shed, as shown in the final snapshot. The stagnation streamline in the high-fidelity results undergoes a marked change of behavior during this final interval, exhibiting a bursting separation bubble that is unrepresented in the low-order model. The high-fidelity results also indicate a growing recirculation zone in the vicinity of the secondary vorticity drawn out of the boundary layer by the LEV; the low-order model is insufficiently rich to predict this behavior.

This tendency to deviate at later times is reflected in the force predictions, as well. The lift and drag predicted by the models at 45°, as shown in Fig. 18, agree reasonably well with the high-fidelity results at early times, but exhibit different trends compared to the high-fidelity results at later times. The impulse matching model predicts both force components better than the Brown–Michael model. Note that the Wagner function predicts the magnitude of lift at the earliest times quite well, but quickly deviates as the leading-edge vortex develops.
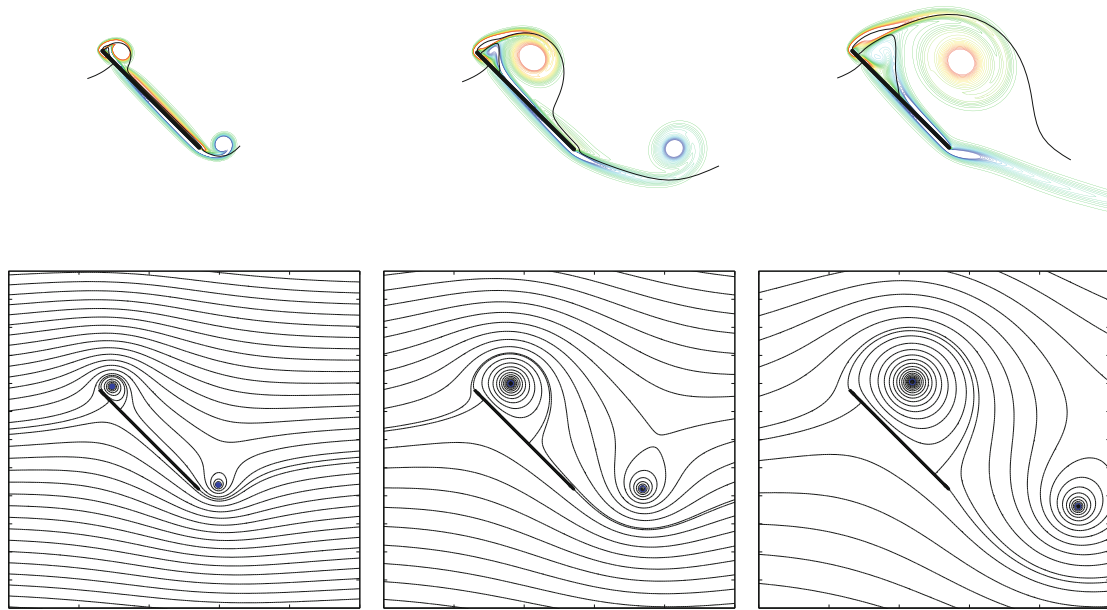
Fig. 17 VVPM vorticity contours (*first row*) and impulse matching model streamlines and point vortex locations (*second row*) for impulsive motion of flat plate at 45° angle of attack. The stagnation streamline is also shown in the VVPM results. *First column* $Ut/c = 0.24$; *second column* $Ut/c = 1$; *third column* $Ut/c = 2.24$ (Color figure online)
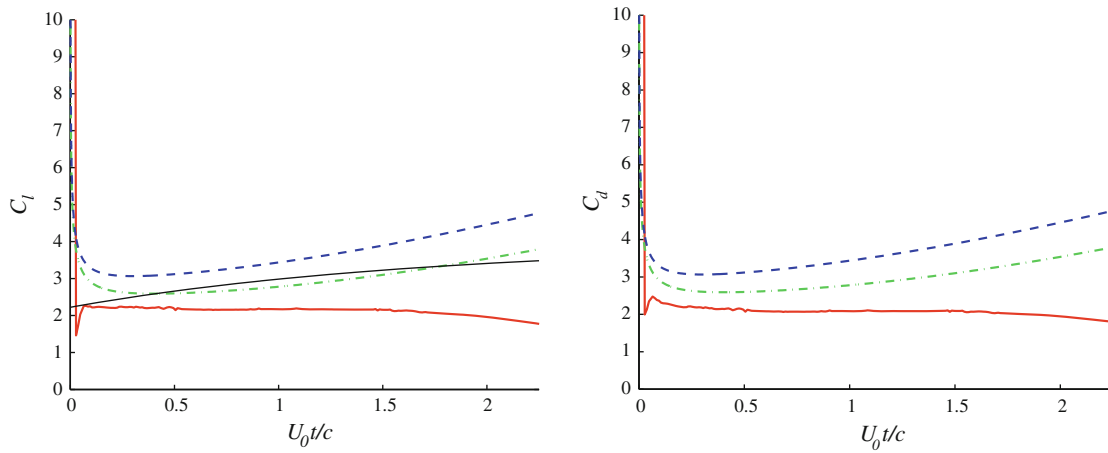

Fig. 18 Lift (*left*) and drag (*right*) coefficients for impulsive motion of flat plate at 45° angle of attack. Impulse matching model (*green dashed line*); Brown–Michael model (*blue dashed line*); VVPM simulation (*red dashed line*); Wagner function (*black dashed line*) (Color figure online)

The development of the symmetric wake at 90° angle of attack is shown in Fig. 19. Again, the point vortices track the locations of the center of vorticity of the high-fidelity results reasonably well for early times, but less so after three chord lengths of travel; the point vortices tend to remain closer to the plate than the wake vortices of the viscous solution. This deviation is also observed in the length of the recirculation region enclosed by the stagnation streamline. The drag comparison, depicted in Fig. 20, exhibits satisfactory agreement between the impulse matching model and the VVPM results, though the drag predicted by the impulse matching model decays more rapidly. The Brown–Michael prediction is consistently larger than the new low-order model.

5 Concluding remarks and extensions of low-order model

The model presented in this work has been shown to predict forces on a two-dimensional pitching or perching plate in reasonably good agreement with corresponding experiments and high-fidelity simulations, particularly
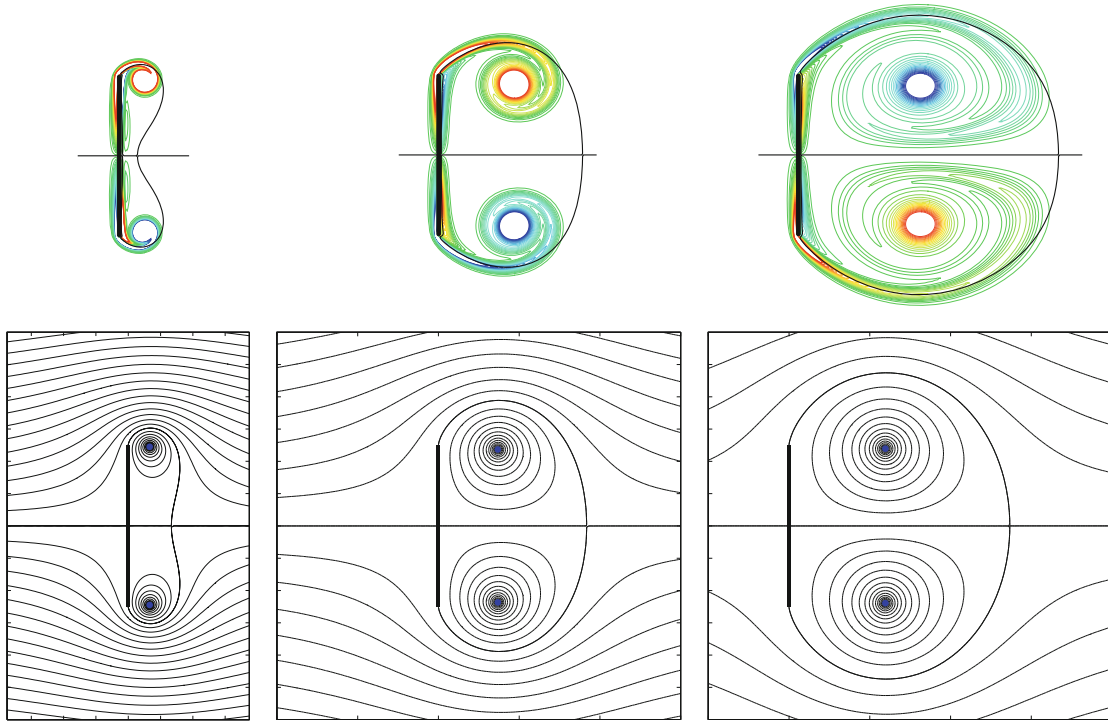
Fig. 19 VVPM vorticity contours (*first row*) and impulse matching model streamlines and point vortex locations (*second row*) for impulsive motion of flat plate at 90° angle of attack. The stagnation streamline is also shown in the VVPM results. *First column* $Ut/c = 0.24$; *second column* $Ut/c = 1$; *third column* $Ut/c = 3$
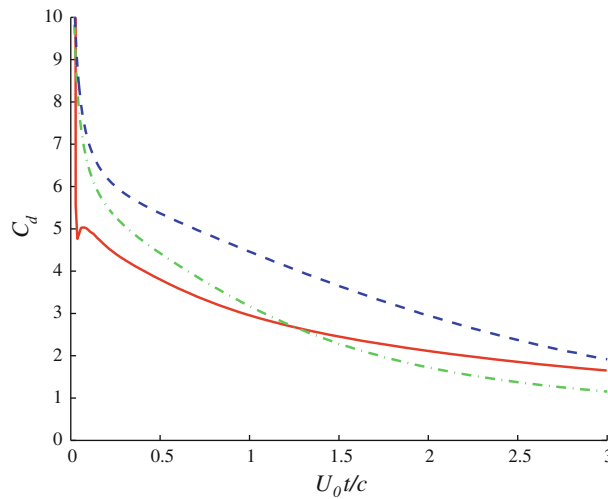

Fig. 20 Drag coefficient for impulsive motion of flat plate at 90° angle of attack. Impulse matching model (*green dashed line*); Brown–Michael model (*blue dashed line*); VVPM simulation (*red dashed line*) (Color figure online)

at high pitch rates. The agreement is notable, considering that fewer than 10° of freedom—compared to 10^5–10^6 for a well-resolved high-fidelity simulation at Reynolds number 1,000—are needed to achieve it. However, there are a number of aspects of the model that should be discussed further.

First, it is natural to consider how the model can be made more accurate. The model, as constructed, can be thought of as a combination of four basic components: (1) shed vorticity is represented as isolated point vortex singularities; (2) vortex strengths are determined by some constraint; (3) each vortex singularity moves according to an evolution equation; (4) a vortex is 'shed' (and a new vortex released) by a criterion on its strength. It is important to note that any of these four components can be altered with little change in the other

three. For example, in this work, we have modified the evolution equation of component (3), but left the other components unchanged. We have seen that this has improved the accuracy of the model.

The accuracy of the model might also be improved by reconsideration of components (1) and (2). For example, the Kutta condition has been used to determine the strengths of the developing point vortices. However, one might replace this condition by determining the strengths empirically, for example, from high-fidelity computations or experiment. In this way, the model becomes a framework for *model reduction*, with an attractive phenomenological foundation. In ongoing work, we are exploring the use of techniques from optimal control and estimation theory in order to determine the vortex circulation (or its rate of change) that best matches the forces on the plate computed from high-fidelity simulations. One might also improve the accuracy of the model by augmenting component (1) with higher-order singularities. Each new singularity would require corresponding conditions to determine its strength; these conditions might be generated from the aforementioned empirical reduction, for example to determine the coefficients of a multipole expansion about the moving singular points.

In this work, we have only demonstrated the model on the development of the leading-edge vortex, and one generally desires capabilities for the model beyond improved accuracy of this start-up behavior. If, for example, we insist on comparable fidelity of the model when the wing is fixed at high angle of attack for longer duration then we would expect the model to capture the bifurcation to sustained vortex shedding [6]. It is not yet clear whether the model, in its present form, can admit similar dynamical behavior; for example, the model was not able to predict the bifurcation from closed to open separation bubble in the case of fixed angle of 45 degrees. Undoubtedly, such behavior is highly dependent on the choice of shedding criterion (component (4) above). As mentioned earlier in this paper, one might instead use a criterion based on the formation number [31] or adapt techniques from dynamical systems theory [27].

Other problems of interest for biologically inspired MAVs require consideration of flapping-wing aerodynamics and, in particular, continuous encounters of a wing with its previously shed vorticity. As these encounters generally involve interactions between a vortex and the attached boundary layer of the wing [15,50], they may not be well captured in a purely inviscid calculation [30]. It is also important to note that, for motions in which the flow remains attached at the leading edge, it is preferable to apply a suction pressure in lieu of a vortex released from that edge. In order to distinguish such cases, one might rely on the criterion recently proposed in [40], in which separation is deemed to occur when this suction pressure exceeds critical bounds that are determined empirically. Note that the Polhamus leading-edge suction analogy is essentially based on this principle [37].

Finally, and crucially, the model must be extended to finite aspect ratio wings for it to be of general use for MAV flight architectures. A natural approach to this extension is via a lifting-line theory, in which the local angle of attack of each wing section is modified by induced velocity from streamwise line vortices supposed to extend from the bound vorticity to the shed vortices. Models for unsteady aerodynamic response in this form have been developed by, for example, Jones [23], and built upon by Dore [10]. In this extension to three-dimensional flows, care must be taken to preserve the simplicity of the model. This is a current target of study by the authors.

Appendix

In this section, we present the derivation of the evolution equation (19) for the impulse matching model. We start with Eq. (18), which expresses the basic principle of the model that the rate of change of the impulse of the actual vortex be identical to that of the constant-strength surrogate vortex. Note that, by the circle theorem, $\zeta_v^{(i)} = 1/\zeta_v^*$, so the left-hand side of (18) can be written as

$$\frac{\mathrm{d}}{\mathrm{d}t}(\zeta_v - \zeta_v^{(i)}) = \frac{\mathrm{d}\zeta_v}{\mathrm{d}t} + \frac{1}{\zeta_v^{*2}} \frac{\mathrm{d}\zeta_v^*}{\mathrm{d}t}. \tag{33}$$

Denote the right-hand side of (18) by f and then note that the complex conjugate of the equation is

$$\frac{\mathrm{d}\zeta_v^*}{\mathrm{d}t} + \frac{1}{\zeta_v^2} \frac{\mathrm{d}\zeta_v}{\mathrm{d}t} = f^*. \tag{34}$$

Eliminate $d\zeta_v^*/dt$ between these equations and substitute f and f^*, to arrive at

$$\frac{d\zeta_v}{dt} = -\left(\frac{\zeta_v^* - 1/\zeta_v}{\zeta_v^* + 1/\zeta_v}\right)\frac{\zeta_v}{\Gamma_v}\frac{d\Gamma_v}{dt} + \frac{d\zeta_v^{CS}}{dt}, \tag{35}$$

where we have used the matching conditions on position and strength between the vortex and its surrogate.

The inverse of the mapping (2),

$$\zeta_v = \tilde{z}_v/a + \sqrt{\tilde{z}_v^2/a^2 - 1}, \tag{36}$$

can be manipulated more clearly if we define $u = \tilde{z}_v/a$. Thus, the vectors from the edges of the plate, $z_v - z_{10}$ and $z_v - z_{20}$, are easily expressed as

$$z_v - z_{10} = ae^{i\alpha}(u - 1), \quad z_v - z_{20} = ae^{i\alpha}(u + 1). \tag{37}$$

For convenience of derivation, we define the factors

$$D_\pm = (u + 1)^{1/2} \pm (u - 1)^{1/2}. \tag{38}$$

It is then easy to verify the relations

$$D_+ D_- = 2, \quad (u \pm 1)^{1/2} = \frac{1}{2}(D_+ \pm D_-), \tag{39}$$

and

$$\frac{dD_+}{dt} = \frac{1}{2}\left[\frac{1}{(u+1)^{1/2}} + \frac{1}{(u-1)^{1/2}}\right]\frac{du}{dt} = \left(\frac{2D_+}{D_+^2 - D_-^2}\right)\frac{du}{dt}, \tag{40}$$

and that the inverse mapping is simply $\zeta_v = D_+^2/2$. Thus,

$$\zeta_v^* \pm 1/\zeta_v = \frac{D_+^{*2}}{2} \pm \frac{2}{D_+^2} = \frac{1}{2}\left(D_+^{*2} \pm D_-^2\right), \tag{41}$$

and

$$\frac{d\zeta_v}{dt} = D_+\frac{dD_+}{dt} = \left(\frac{2D_+^2}{D_+^2 - D_-^2}\right)\frac{du}{dt}. \tag{42}$$

Similarly,

$$\frac{d\zeta_v^{CS}}{dt} = \left(\frac{2D_+^2}{D_+^2 - D_-^2}\right)\frac{du^{CS}}{dt}, \tag{43}$$

where $u^{CS} = \tilde{z}_v^{CS}/a$. Thus, the evolution equation in terms of u is

$$\frac{du}{dt} + \frac{1}{4}\frac{(D_+^2 - D_-^2)(D_+^{*2} - D_-^2)}{(D_+^{*2} + D_-^2)}\frac{1}{\Gamma_v}\frac{d\Gamma_v}{dt} = \frac{du^{CS}}{dt}. \tag{44}$$

Now, note that $D_+^{*2} \pm D_-^2 = \frac{1}{2}D_+^* D_-(D_+ D_+^* \pm D_- D_-^*)$, so that the evolution equation can be written as

$$\frac{du}{dt} + \frac{1}{4}(D_+^2 - D_-^2)\left(\frac{D_+ D_+^* - D_- D_-^*}{D_+ D_+^* + D_- D_-^*}\right)\frac{1}{\Gamma_v}\frac{d\Gamma_v}{dt} = \frac{du^{CS}}{dt}. \tag{45}$$

Expanding the numerator and denominator of the ratio in parentheses as follow,

$$D_+ D_+^* \pm D_- D_-^* = \frac{1}{2}(D_+ \pm D_-)(D_+^* + D_-^*) + \frac{1}{2}(D_+ \mp D_-)(D_+^* - D_-^*), \tag{46}$$

substituting into (45) and combining terms, we can write the equation as

$$\frac{\mathrm{d}u}{\mathrm{d}t} + \frac{|u+1|(u-1) + |u-1|(u+1)}{|u+1| + |u-1|} \frac{1}{\Gamma_v} \frac{\mathrm{d}\Gamma_v}{\mathrm{d}t} = \frac{\mathrm{d}u^{CS}}{\mathrm{d}t}. \tag{47}$$

We would like to express this in terms of z_v. Note that, from equation (1),

$$\frac{\mathrm{d}z_v}{\mathrm{d}t} = \frac{\mathrm{d}z_c}{\mathrm{d}t} + a\frac{\mathrm{d}u}{\mathrm{d}t}\mathrm{e}^{\mathrm{i}\alpha} + i\Omega\tilde{z}_v\mathrm{e}^{\mathrm{i}\alpha}. \tag{48}$$

Since, by construction, the surrogate vortex is subjected to the same body kinematics, then z_v^{CS} satisfies the same equation (with $\mathrm{d}u/\mathrm{d}t$ replaced by $\mathrm{d}u^{CS}/\mathrm{d}t$). Thus,

$$\frac{\mathrm{d}u}{\mathrm{d}t} - \frac{\mathrm{d}u^{CS}}{\mathrm{d}t} = \frac{1}{a\mathrm{e}^{\mathrm{i}\alpha}}\left(\frac{\mathrm{d}z_v}{\mathrm{d}t} - \frac{\mathrm{d}z_v^{CS}}{\mathrm{d}t}\right), \tag{49}$$

and, with the help of Eqs. (16) and (37), we arrive at our final result,

$$\frac{\mathrm{d}z_v}{\mathrm{d}t} + \frac{h(z_v - z_{10}, z_v - z_{20})}{\Gamma_v}\frac{\mathrm{d}\Gamma_v}{\mathrm{d}t} = W_{-v}^*(z_v), \tag{50}$$

where

$$h(v, w) = \frac{|v|w + |w|v}{|v| + |w|}. \tag{51}$$

References

1. Alben, S., Shelley, M.J.: Flapping states of a flag in an inviscid fluid: bistability and the transition to chaos. Phys. Rev. Lett. **100**, 074301 (2008)
2. Ansari, S.A., Zbikowski, R., Knowles, K.: Non-linear unsteady aerodynamic model for insect-like flapping wings in the hover. Part 1: methodology and analysis. Proc. IMechE Part G J. Aerosp. Eng. **220**, 61–83 (2006)
3. Ansari, S.A., Zbikowski, R., Knowles, K.: Non-linear unsteady aerodynamic model for insect-like flapping wings in the hover. Part 2: implementation and validation. Proc. IMechE Part G J. Aerosp. Eng. **220**, 169–186 (2006)
4. Berman, G.J., Wang, Z.J.: Energy-minimizing kinematics in hovering insect flight. J. Fluid Mech. **582**, 153–168 (2007)
5. Brown, C.E., Michael, W.H.: Effect of leading edge separation on the lift of a delta wing. J. Aerosp. Sci. **21**, 690–694 (1954)
6. Chen, K.K., Colonius, T., Taira, K.: The leading-edge vortex and quasisteady vortex shedding on an accelerating plate. Phys. Fluids **22**(3), 033601 (2010)
7. Clements, R.R.: An inviscid model for two-dimensional vortex shedding. J. Fluid Mech. **57**(2), 321–336 (1973)
8. Cortelezzi, L., Leonard, A.: Point vortex model of the unsteady separated flow past a semi-infinite plate with transverse motion. Fluid Dyn. Res. **11**, 263–295 (1993)
9. Davis, C.I.R., Shajiee, S., Mohseni, K.: Lift Enhancement in a Flapping Airfoil by an Attached Free Vortex and Sink. AIAA Paper 2009-0390 (2009)
10. Dore, B.D.: The Unsteady Forces on Finite Wings in Transient Motion. Technical report 3456. Aeronautical Research Council (1966)
11. Edwards, R.H.: Leading edge separation from delta wings. J. Aerosp. Sci. **21**, 134–135 (1954)
12. Eldredge, J., Wang, C.: High-Fidelity Simulations and Low-Order Modeling of a Rapidly Pitching Plate. AIAA Paper 2010-4281, 40th AIAA Fluid Dynamics Conference, Chicago (2010)
13. Eldredge, J.D.: Numerical simulation of the fluid dynamics of 2D rigid body motion with the vortex particle method. J. Comput. Phys. **221**, 626–648 (2007)
14. Eldredge, J.D.: A reconciliation of viscous and inviscid approaches to computing locomotion of deforming bodies. Exp. Mech. **50**(9), 1349–1353 (2009)
15. Eldredge, J.D., Toomey, J., Medina, A.: On the roles of chord-wise flexibility in a flapping wing with hovering kinematics. J. Fluid Mech. **659**, 94–115 (2010)
16. Eldredge, J.D., Wang, C., Ol, M.V.: A Computational Study of a Canonical Pitch-up, Pitch-down Wing Maneuver. AIAA Paper 2009-3687 (2009)
17. Gendrich, C.P., Koochesfahani, M.M., Visbal, M.R.: Effects of initial acceleration on the flow field development around rapidly pitching airfoils. J. Fluids Eng. **117**, 45–49 (1995)
18. Graham, J.M.R.: The forces on sharp-edged cylinders in oscillatory flow at low Keulegan–Carpenter numbers. J. Fluid Mech. **97**(1), 331–346 (1980)
19. Granlund, K., Ol, M.V., Garmann, D.J., Visbal, M.R., Bernal, L.: Experiments and Computations on Abstractions of Perching. AIAA Paper 2010-4943, 28th AIAA Applied Aerodynamic Conference, Chicago (2010)
20. Grauer, J., Ulrich, E., Hubbard, J., Pines, D., Humbert, J.S.: Testing and system identification of an ornithopter in longitudinal flight. J. Aircr. **48**(2), 660–667 (2010)
21. Jones, K.D., Platzer, M.F.: Flapping-Wing Propulsion for a Micro Air Vehicle. AIAA Paper 2000-0897 (2000)

22. Jones, M.A.: The separated flow of an inviscid fluid around a moving flat plate. J. Fluid Mech. **496**, 405–441 (2003)
23. Jones, R.T.: The Unsteady Lift of a Wing of Finite Aspect Ratio. Technical report 681, NACA (1939)
24. Katz, J., Weihs, D.: Behavior of vortex wakes from oscillating airfoils. AIAA J. **15**(12), 861–863 (1978)
25. Koochesfahani, M.M., Smiljanovski, V.: Initial acceleration effects on flow evolution around airfoils pitching to high angles of attack. AIAA J. **31**(8), 1529–1531 (1993)
26. Krasny, R.: Vortex sheet computations: roll-up, wake, separation. In: Lectures in Applied Mathematics, vol. 28, pp. 385–402. AMS (1991)
27. Krechetnikov, R., Marsden, J.E., Nagib, H.M.: A low-dimensional model of separation bubbles. Phys. D **238**, 1152–1160 (2009)
28. McCroskey, W.J.: Unsteady airfoils. Ann. Rev. Fluid Mech. **14**, 285–311 (1982)
29. Michelin, S., Llewellyn Smith, S.G.: An unsteady point vortex method for coupled fluid–solid problems. Theor. Comput. Fluid Dyn. **23**, 127–153 (2009)
30. Michelin, S., Llewellyn Smith, S.G.: Falling cards and flapping flags: understanding fluid–solid interactions using an unsteady point vortex model. Theor. Comput. Fluid Dyn. **24**, 195–200 (2010)
31. Milano, M., Gharib, M.: Uncovering the physics of flapping flat plates with artificial evolution. J. Fluid Mech. **534**, 403–409 (2005)
32. Milne-Thomson, L.M.: Theoretical Hydrodynamics. Dover Publications, Inc., New York (1996)
33. Mourtos, N.J., Brooks, M.: Flow past a flat plate with a vortex/sink combination. J. Appl. Mech. **63**, 543–550 (1996)
34. Nitsche, M., Krasny, R.: A numerical study of vortex ring formation at the edge of a circular tube. J. Fluid Mech. **276**, 139–161 (1994)
35. Ol, M.V., Eldredge, J.D., Wang, C.: High-amplitude pitch of a flat plate: an abstraction of perching and flapping. Int. J. Micro Air Veh. **1**(3), 203–216 (2009)
36. Pitt Ford, C.W., Babinsky, H.: Lift and the Leading Edge Vortex. AIAA Paper 2012-0911 (2012)
37. Polhamus, E.C.: A Concept of the Vortex Lift of Sharp-Edge Delta Wings Based on a Leading-Edge-Suction Analogy. Technical report TN D-3767, NASA (1966)
38. Pullin, D.I.: The large-scale structure of unsteady self-similar rolled-up vortex sheets. J. Fluid Mech. **88**(3), 401–430 (1978)
39. Pullin, D.I., Wang, Z.J.: Unsteady forces on an accelerating plate and application to hovering insect flight. J. Fluid Mech. **509**, 1–21 (2004)
40. Ramesh, K., Gopalarathnam, A., Ol, M.V., Granlund, K., Edwards, J.R.: Augmentation of Inviscid Airfoil Theory to Predict and Model 2d Unsteady Vortex Dominated Flows. AIAA Paper 2011-3578 (2011)
41. Rossow, V.J.: Lift enhancement by an externally trapped vortex. J. Aircr. **15**(9), 618–625 (1978)
42. Saffman, P.G., Sheffield, J.S.: Flow over a wing with an attached free vortex. Stud. Appl. Math. **57**, 107–117 (1977)
43. Sedov, L.I.: Two-Dimensional Problems in Hydrodynamics and Aerodynamics. New York, London (1965)
44. Shukla, R.K., Eldredge, J.D.: An inviscid model for vortex shedding from a deforming body. Theor. Comput. Fluid Dyn. **21**, 343–368 (2007)
45. Tchieu, A.A., Leonard, A.: A discrete-vortex model for the arbitrary motion of a thin airfoil with fluidic control. J. Fluids Struct. **27**(5–6), 680–693 (2011) (submitted)
46. Theodorsen, T.: General Theory of Aerodynamic Instability and the Mechanism of Flutter. TR-496, NACA (1935)
47. Visbal, M.R.: Dynamic stall of a constant-rate pitching airfoil. J. Aircr. **27**(5), 400–407 (1990)
48. von Kármán, T., Sears, W.R.: Airfoil theory for non-uniform motion. J. Aeronaut. Sci. **5**(10), 379–390 (1938)
49. Wagner, H.: Über die Entstehung des dynamischen Auftriebes von Tragflügeln. Zeitschrift für Angewandte Mathematik und Mechanik **5**(1), 17–35 (1925)
50. Wang, Z.J., Birch, J.M., Dickinson, M.H.: Unsteady forces and flows in low Reynolds number hovering flight: two dimensional computations vs robotic wing experiments. J. Exp. Biol. **207**, 449–460 (2004)